nature nanotechnology

LETTERS

https://doi.org/10.1038/s41565-018-0297-6

Corrected: Author Correction

Robust topologically protected transport in photonic crystals at telecommunication wavelengths

Mikhail I. Shalaev[1], Wiktor Walasik[1], Alexander Tsukernik[2], Yun Xu[1,3] and Natalia M. Litchinitser[1]*

Photonic topological insulators offer the possibility to eliminate backscattering losses and improve the efficiency of optical communication systems. Despite considerable efforts, a direct experimental demonstration of theoretically predicted robust, lossless energy transport in topological insulators operating at near-infrared frequencies is still missing. Here, we combine the properties of a planar silicon photonic crystal and the concept of topological protection to design, fabricate and characterize an optical topological insulator that exhibits the valley Hall effect. We show that the transmittances are the same for light propagation along a straight topological interface and one with four sharp turns. This result quantitatively demonstrates the suppression of backscattering due to the non-trivial topology of the structure. The photonic-crystal-based approach offers significant advantages compared with other realizations of photonic topological insulators, such as lower propagation losses, the presence of a band gap for light propagating in the crystal-slab plane, a larger operating bandwidth, a much smaller footprint, compatibility with complementary metal–oxide–semiconductor fabrication technology, and the fact that it allows for operation at telecommunications wavelengths.

Topological insulators are materials that insulate in the bulk, but conduct along the edge, and could advance fields ranging from condensed matter physics[1–7] to acoustics[8] and photonics[9–15]. The first photonic analogue of a quantum Hall topological insulator was realized in the microwave regime using gyromagnetic materials, and a strong magnetic field to break the time-reversal symmetry[16]. Later, non-magnetic quantum Hall topological insulators mimicking time-reversal-symmetry breaking were demonstrated at near-infrared frequencies using lattices of coupled waveguides[14] and ring resonators[13]. Light transmissions of coupled-ring-resonator systems with different dimensionalities, trivial one-dimensional and topological two-dimensional (2D) lattices were compared in ref. [17]. In addition, photonic analogues of the spin and valley Hall effects that require spatial rather than temporal symmetries to be broken have been proposed and demonstrated in the microwave frequency range in photonic crystals made of metallic[18–21] or dielectric[22–26] materials. Finally, strong light–matter interactions between topologically robust photonic edge states and single quantum emitters have been demonstrated in the near-infrared frequency range[15].

We compare light propagation along a straight topological interface and an interface with sharp turns, to directly measure the robust energy transport and quantitatively characterize the suppression of the backscattering. Coupling of light between a standard silicon wire waveguide and a topological edge state is challenging due to the mismatch of their field profiles. Here, the characterization was enabled by optimization of the coupling geometry leading to input-to-output coupling of light with an efficiency above 70% (see Supplementary Information, section C). In previous demonstrations[13,14], significant scattering losses prevented the direct characterization of the light transmission efficiency. The topological system of coupled-ring resonators[13] was characterized by −20 dB losses due to mismatched resonant frequencies of individual micro-rings caused by fabrication imperfections. The photonic-crystal-based approach offers several advantages over the other realizations. First, light propagation in photonic crystals exhibits very low losses[27], which enables us to demonstrate essentially the same transmittance in the structures with the straight interface and an interface featuring four sharp turns. Such a property is especially important for the realization of efficient passive devices. Second, the photonic crystal slab exhibits a band gap that does not allow for in-plane scattering, and light propagation is only allowed in the topologically protected edge states. In contrast, other approaches[13,14] do not feature a band gap for the in-plane propagation. Instead, the band gap is only present for light guided inside ring resonators or helical waveguides; that is, light scattered from the waveguide can propagate in the quasi-crystal plane. Moreover, the bandwidth of our photonic-crystal-based design—a gap/mid-gap ratio of approximately 5%—is much larger compared with less than 0.01% reported for the coupled-ring-resonator approach[13]. Finally, the photonic-crystal-based approach offers a compact footprint suitable for complementary metal–oxide–semiconductor integration, and features a unit cell size roughly 100 times smaller than reported in ref. [13]. The photonic crystal realization allows us to observe topological effects on a micrometre-scale size, while the approach based on coupled helical waveguides requires a centimetre-long propagation[14]. All the advantages mentioned above make the photonic crystal platform a promising candidate for the future implementation of topological silicon photonics, ultrahigh-bit-rate communications systems, and classical and quantum computing.

Figure 1a shows a schematic of a photonic-crystal-based valley Hall topological insulator operating at telecommunications wavelengths, implemented on a silicon platform. The photonic crystal structure is built from unit cells shown in the inset of Fig. 1b and consists of a honeycomb lattice with two inverted equilateral triangular air holes per unit cell. Here, we consider only the transverse-electric-like polarized light[28] propagating in the x–y plane and

[1]Department of Electrical and Computer Engineering, Duke University, Durham, NC, USA. [2]Toronto Nanofabrication Centre, University of Toronto, Toronto, Ontario, Canada. [3]Department of Electrical Engineering, University at Buffalo, The State University of New York, Buffalo, NY, USA.
*e-mail: natalia.litchinitser@duke.edu

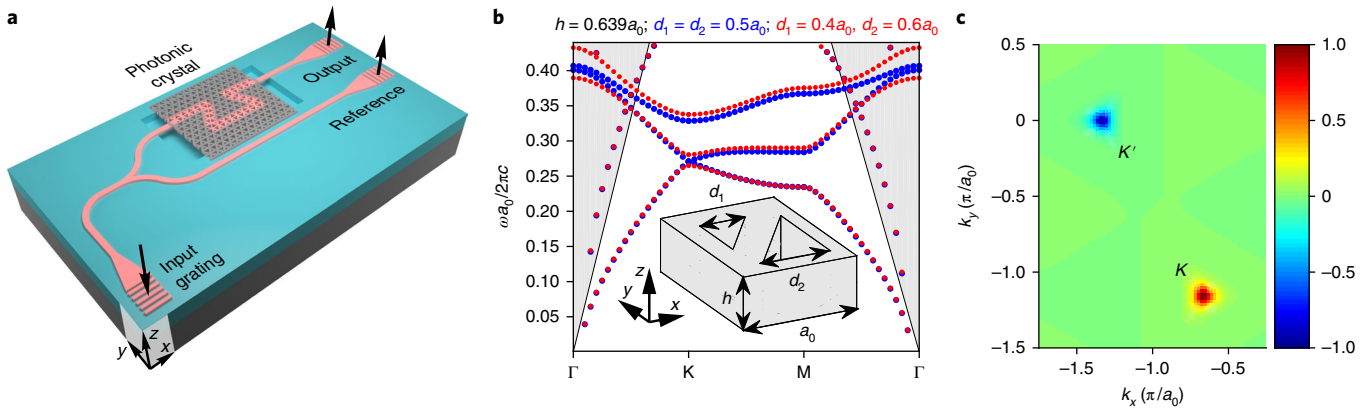

Fig. 1 | Schematic and operation principles of the photonic-crystal-based topological insulator. a, Schematic of the proposed structure. The photonic crystal is surrounded by air at the top and bottom (along the *z* axis). Light is coupled into the chip by the input grating followed by a taper. The energy is split between the two arms: one couples light into the photonic crystal structure, while the other leads directly to the reference grating. The light transmitted through the photonic crystal is out-coupled by the output grating. Silicon is shown in grey and silicon dioxide in cyan. **b**, Band structures of the photonic crystal slab with C_6 symmetry (blue) versus C_3 symmetry exhibiting the valley Hall effect (red). Γ, K and M denote the high-symmetry points in the momentum space. The frequencies ω above the light cone are shaded in grey. The speed of light in vacuum is denoted by *c*. The inset illustrates the unit cell of the photonic crystal slab and shows the dimensions of the structure. **c**, Normalized Berry curvature of the first band of the C_3-symmetric photonic crystal lattice in the momentum space spanned by the wavevector $\mathbf{k} = [k_x, k_y]$. The valley Chern numbers $C^{K/K'} = \pm ½$ correspond to the *K*/*K*′ valleys.

confined in the *z* direction by the total internal reflection. The starting point of our design is a photonic crystal lattice with a C_6 symmetry, having equal hole sizes $d_1 = d_2$, and featuring a Dirac cone at the *K* and *K*′ points in the momentum space, as shown by the blue points in Fig. 1b. The introduction of asymmetry between the sizes of the two holes within the unit cell ($d_1 \neq d_2$) breaks the inversion symmetry and reduces the lattice symmetry to C_3. As a result, the degeneracy at the *K* (*K*′) point is lifted and a band gap opens, as shown by the red points in Fig. 1b. A similar behaviour of the band structure was recently observed in a photonic boron-nitride lattice built of circular instead of triangular holes[29]. The advantage of the design with triangular holes is a direct and, most importantly, larger band gap at the *K* point, for the same strength of the symmetry-breaking perturbation[30], compared with other proposed geometries. This is especially important for photonic crystals with a small hole-size asymmetry, and for the case of low refractive-index contrast between the slab and surrounding medium.

The parameters of the structure, such as the lattice constant a_0, hole sizes d_1 and d_2, and slab height *h*, are optimized to ensure that: (1) the structure operates in the telecommunications wavelength range; (2) the Dirac cone is well defined or a direct band gap is opened; and (3) the thickness *h* is not too large, so that the higher-order modes of the slab (in the out-of-plane direction) are not supported, eliminating the associated losses (for details, see Supplementary Information, section A). The following structure parameters were used in this work: $a_0 = 423$ nm, $h = 0.639a_0$, $d_1 = 0.4a_0$ and $d_2 = 0.6a_0$.

The proposed structure features a non-zero Berry curvature, with opposite signs at the *K* and *K*′ points. The distribution of the normalized Berry curvature Ω for the lowest-energy band computed using the numerical plane wave expansion method is shown in Fig. 1c. We calculated the valley Chern numbers for the first band[31,32] based on the Berry curvature shown in Fig. 1c, and on the analytical description of the system by the Hamiltonian $\hat{H}_{K/K'} = \pm v_D(\sigma_x \delta k_x + \sigma_y \delta k_y) \pm \gamma \sigma_z$ (refs [11,23]). Here, v_D is proportional to the group velocity, $\delta\mathbf{k} = \mathbf{k} - \mathbf{K}$ is the reciprocal vector with respect to the *K* point, γ denotes the strength of the symmetry-breaking perturbation, and $\sigma_{x,y,z}$ denote the Pauli matrices. The valley Chern numbers are given by $C^{K/K'} = \frac{1}{2\pi}\int_{\mathrm{HBZ}_{K/K'}} \Omega(\mathbf{k}) \mathrm{d}^2k = \pm 1/2$, where the integration is carried over half of the first Brillouin zone (HBZ) around the *K* or *K*′ points (for details, see Supplementary Information, section B).

For the valley Hall effect, edge states exist at the interface between the structures with two different 'polarities', which in our case are determined by the orientation of the large triangle, pointing up (Δ) or down (∇). The difference between the valley Chern numbers across the interface is given by $|\Delta C^{K/K'}| = |C_\nabla^{K/K'} - C_\Delta^{K/K'}| = 1$, and determines the number of edge states in each valley. Figure 2a shows the band structure for a photonic crystal with such an interface. In the upper half of the photonic crystal structure, the large triangles are pointing upwards, while in the lower half of the photonic crystal, the large triangles are pointing downwards. The band structure reveals the presence of a helical edge state (magenta) crossing the band gap (shaded in green) between the first and second bulk bands (blue). The group velocity for the edge state is nearly constant within the band gap, and the effects of the group-velocity dispersion do not play a significant role for this state. As the band structure is symmetric with respect to the wave vector k_x, there is a time-reversed partner edge state with opposite group velocity and opposite helicity in the second valley.

To quantitatively prove the valley Hall topological protection for these edge states, we study the propagation of light along an interface with sharp turns. We consider a trapezoidally shaped interface between the photonic crystal parts with opposite 'polarities' shown in Fig. 2b. The resulting transmittance is illustrated in Fig. 2d and clearly reveals a region with a unitary transmittance. This result proves that the propagation of light along the interface between the photonic crystals with opposite 'polarities' is topologically protected against scattering on sharp turns. A typical normalized energy-density distribution along the interface is shown in Fig. 2c.

Generally, valley Hall topologically protected edge states are robust against defects that do not couple states with opposite helicities. In the case of topologically protected states, the field distributions of the forward- and backward-propagating states show vortex-like characteristics with opposite helicities reflecting the broken inversion symmetry[33]. Therefore, the field distributions of counter-propagating states do not overlap and, as a result, the back-scattering is suppressed in systems exhibiting the photonic analogue of the valley Hall effect. However, defects that efficiently couple states with opposite helicities may appear accidentally due to fabrication errors. Such defects must have specific scattering properties,

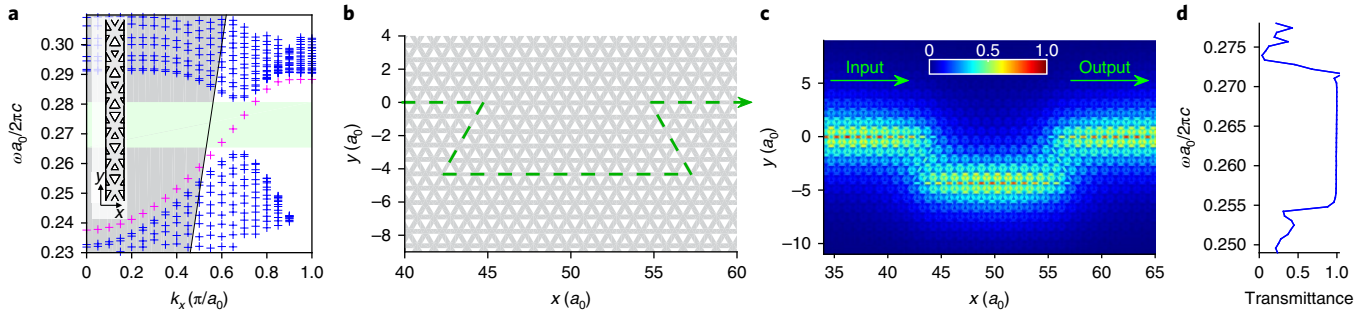

Fig. 2 | Scattering-free edge state in the photonic-crystal-based topological insulator. a, Band diagram showing the edge state of the periodic 3D structure illustrated in the inset. The structure is periodic along the *x* direction and finite along the *y* axis (20 unit cells of each region), and has the thickness *h* along the *z* axis. The frequencies above the light cone are shaded in grey. The edge state (magenta) crosses the band gap (green) between the bulk bands (blue). **b**, Central part of the 2D photonic crystal with a trapezoidally shaped interface used in transmittance studies. **c**, A typical normalized energy-density distribution of the propagating edge state for the frequency $\omega a_0/2\pi c = 0.263$ located inside the band gap. **d**, Transmittance spectrum of the structure shown in **b**.

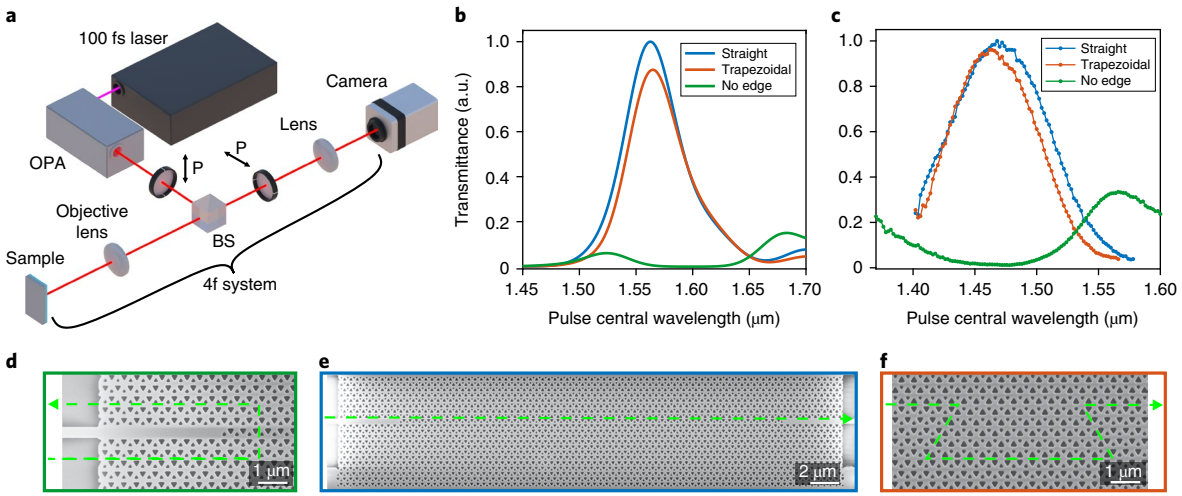

Fig. 3 | Observation of topologically protected propagation in a photonic-crystal-based topological insulator. a, Experimental setup used for the transmittance measurements. Arrows indicate the polarization direction of the polarizers (P). BS, beam splitter; OPA, optical parametric amplifier. **b**,**c**, Numerically computed (**b**) and experimentally measured transmittances (**c**) for: the structure with a photonic crystal having a single 'polarity' without an interface (green line); the structure with the straight interface (blue line); and the structure with the trapezoidal interface (red line). **d**–**f**, Scanning electron microscopy images showing the photonic crystal slabs, including a sample containing only a single 'polarity' (**d**), and samples composed of two parts with opposite 'polarities' separated by either a straight interface (**e**) or a trapezoidal interface (**f**). Predicted paths of the light propagation are shown schematically by green arrows.

enabling the coupling of opposite pseudo-spin states, and therefore the probability of their appearance is lower than for other defects.

Next, we fabricated the samples and performed transmission measurements for topological edge states (for details, see the Methods and Supplementary Information, section D). The experimental setup is shown schematically in Fig. 3a. The transmittance of the photonic crystal structures shown in Fig. 3d–f is calculated as a ratio between the light transmitted through the photonic crystal and the reference and then normalized to its maximum. To collect the spectral dependence of the transmittance, the central frequency of the source was swept between 1,350 and 1,600 nm. The resulting transmittance is shown in Fig. 3c. The experimentally measured transmittance curves are smooth due to the large spectral width of the probing pulse (a full width at half maximum of around 40 nm). Therefore, the measured transmittance is the convolution of the real transmittance of the sample and the spectral shape of the pulse.

We performed experiments on three different samples, in which: (1) only one 'polarity' of the crystal existed (Fig. 3d); (2) there was a straight interface between the crystal parts with opposite 'polarities' (no sharp turns; Fig. 3e); and (3) there was a trapezoidally shaped interface (Fig. 3f). We observed that for the sample with no edge, there was a region of low transmittance (for the wavelength range 1,420–1,510 nm), revealing the presence of a band gap. These measurements allowed us to estimate that the size of the band gap was around 75 nm. The spectral measurements of the samples with an interface showed high transmittance in the band-gap region, proving the existence of an edge state. Importantly, the transmittances of the samples with straight and trapezoidal interfaces presented very similar spectral dependencies. This confirmed our theoretical prediction that the propagating edge state is immune to scattering at sharp turns and proves the topological protection of the excited edge states[18]. The transmittance for the sample with the trapezoidal interface was slightly lower than for the sample with the straight interface due to the limited width of the photonic crystal structure in the *y* direction (for details, see Supplementary Information, section C). The size of the structure was limited to avoid bending of the

suspended photonic crystal slab that might occur during the drying process after etching of the silicon dioxide layer.

Transmission measurements were reproduced using numerical simulations of the structures studied experimentally. The propagation of light was simulated in the three types of structure shown in Fig. 3d–f with the same dimensions as those of the fabricated samples. The numerically computed transmittances presented in Fig. 3b are in good agreement with the experimental results.

To conclude, we designed and experimentally demonstrated a silicon-based complementary metal–oxide–semiconductor compatible structure that exhibits the valley Hall effect at telecommunications wavelengths. Robust transport was observed by a direct and quantitative comparison of the light transmitted along a topological interface with four sharp turns and a straight interface. The measured transmittances of these two structures were essentially the same, confirming the suppression of backscattering and robust topological transport. The realization of topological insulators in a photonic crystal platform is advantageous as it features low propagation losses, the presence of a band gap, a large operating bandwidth and a small footprint. In addition, the efficient coupling of light to the edge state reported in this work, combined with standard fabrication techniques, makes photonic crystals an ideal platform for the realization of integrated topological photonics that may find applications in the next generation of optical telecommunications systems.

Note added in proof: During the revision of this manuscript, we became aware of a closely related work on valley Hall topological insulators[26].

Online content

Any methods, additional references, Nature Research reporting summaries, source data, statements of data availability and associated accession codes are available at https://doi.org/10.1038/s41565-018-0297-6.

Received: 28 May 2018; Accepted: 5 October 2018;
Published online: 12 November 2018

References

1. Kane, C. L. & Mele, E. J. Z2 topological order and the quantum spin Hall effect. *Phys. Rev. Lett.* **95**, 146802 (2005).
2. Kane, C. L. & Mele, E. J. Quantum spin Hall effect in graphene. *Phys. Rev. Lett.* **95**, 226801 (2005).
3. Moore, J. E. The birth of topological insulators. *Nature* **464**, 194–198 (2010).
4. Bernevig, A. B. & Hughes, T. L. *Topological Insulators and Topological Superconductors* (Princeton Univ. Press, Princeton, 2013).
5. Ferreira, G. J. & Loss, D. Magnetically defined qubits on 3D topological insulators. *Phys. Rev. Lett.* **111**, 106802 (2013).
6. Katmis, F. et al. A high-temperature ferromagnetic topological insulating phase by proximity coupling. *Nature* **533**, 513–516 (2016).
7. Jotzu, G. et al. Experimental realization of the topological haldane model with ultracold fermions. *Nature* **515**, 237–240 (2014).
8. Lu, J. et al. Observation of topological valley transport of sound in sonic crystals. *Nat. Phys.* **13**, 369–375 (2016).
9. Umucalılar, R. O. & Carusotto, I. Artificial gauge field for photons in coupled cavity arrays. *Phys. Rev. A* **84**, 043804 (2011).
10. Hafezi, M., Demler, E. A., Lukin, M. D. & Taylor, J. M. Robust optical delay lines with topological protection. *Nat. Phys.* **7**, 907–912 (2011).
11. Khanikaev, A. B. et al. Photonic topological insulators. *Nat. Mater.* **12**, 233–239 (2012).
12. Fang, K. J., Yu, Z. F. & Fan, S. H. Realizing effective magnetic field for photons by controlling the phase of dynamic modulation. *Nat. Photon.* **6**, 782–787 (2012).
13. Hafezi, M., Mittal, S., Fan, J., Migdall, A. & Taylor, J. M. Imaging topological edge states in silicon photonics. *Nat. Photon.* **7**, 1001–1005 (2013).
14. Rechtsman, M. C. et al. Photonic Floquet topological insulators. *Nature* **496**, 196–200 (2013).
15. Barik, S. et al. A topological quantum optics interface. *Science* **359**, 666–668 (2018).
16. Wang, Z., Chong, Y., Joannopoulos, J. D. & Soljačić, M. Observation of unidirectional backscattering-immune topological electromagnetic states. *Nature* **461**, 772–775 (2009).
17. Mittal, S. et al. Topologically robust transport of photons in a synthetic gauge field. *Phys. Rev. Lett.* **113**, 087403 (2014).
18. Chen, W. J. et al. Experimental realization of photonic topological insulator in a uniaxial metacrystal waveguide. *Nat. Commun.* **5**, 5782 (2014).
19. Ma, T., Khanikaev, A. B., Mousavi, S. H. & Shvets, G. Guiding electromagnetic waves around sharp corners: topologically protected photonic transport in metawaveguides. *Phys. Rev. Lett.* **114**, 127401 (2015).
20. Ma, T. & Shvets, G. Scattering-free edge states between heterogeneous photonic topological insulators. *Phys. Rev. B* **95**, 165102 (2017).
21. Wu, X. et al. Direct observation of valley-polarized topological edge states in designer surface plasmon crystals. *Nat. Commun.* **8**, 1304 (2017).
22. Wu, L. H. & Hu, X. Scheme for achieving a topological photonic crystal by using dielectric material. *Phys. Rev. Lett.* **114**, 223901 (2015).
23. Ma, T. & Shvets, G. All-Si valley-Hall photonic topological insulator. *New J. Phys.* **18**, 025012 (2016).
24. Chen, X.-D., Zhao, F.-L., Chen, M. & Dong, J.-W. Valley-contrasting physics in all-dielectric photonic crystals: orbital angular momentum and topological propagation. *Phys. Rev. B* **96**, 020202 (2017).
25. Dong, J.-W., Chen, X.-D., Zhu, H., Wang, Y. & Zhang, X. Valley photonic crystals for control of spin and topology. *Nat. Mater.* **16**, 298–302 (2016).
26. He, X.-T. et al. Silicon-on-insulator slab for topological valley transport. Preprint at https://arxiv.org/abs/1805.10962 (2018).
27. Dulkeith, E., McNab, S. J. & Vlasov, Y. A. Mapping the optical properties of slab-type two-dimensional photonic crystal waveguides. *Phys. Rev. B* **72**, 115102 (2005).
28. Joannopoulos, J. D., Johnson, S. G., Winn, J. N. & Meade, R. D. *Photonic Crystals Molding the Flow of Light* 2nd edn (Princeton Univ. Press, Princeton, 2008).
29. Collins, M. J., Zhang, F., Bojko, R., Chrostowski, L. & Rechtsman, M. C. Integrated optical Dirac physics via inversion symmetry breaking. *Phys. Rev. A.* **94**, 063827 (2016).
30. Barik, S., Miyake, H., DeGottardi, W., Waks, E. & Hafezi, M. Two-dimensionally confined topological edge states in photonic crystals. *New J. Phys.* **18**, 113013 (2016).
31. Fukui, T., Hatsugai, Y. & Suzuki, H. Chern numbers in discretized Brillouin zone: efficient method of computing (spin) Hall conductances. *J. Phys. Soc. Jpn* **74**, 1674–1677 (2005).
32. Bleu, O., Solnyshkov, D. D. & Malpuech, G. Quantum valley Hall effect and perfect valley filter based on photonic analogs of transitional metal dichalcogenides. *Phys. Rev. B* **95**, 235431 (2017).
33. Shalaev, M. I., Desnavi, S., Walasik, W. & Litchinitser, N. M. Reconfigurable topological photonic crystal. *New J. Phys.* **20**, 023040 (2018).

Acknowledgements

This work was supported by Army Research Office grants W911NF-15-1-0152 and W911NF-11-1-0297. The authors acknowledge discussions with A. Khanikaev.

Author contributions

M.I.S. and N.M.L. proposed the initial idea. M.I.S. and W.W. designed and performed the analytical and numerical analysis of the structure. M.I.S. fabricated the sample, performed the experimental measurements and analysed the results. A.T. and Y.X. assisted with the fabrication and measurement process of the sample. W.W., M.I.S. and N.M.L. co-wrote the manuscript. N.M.L. supervised the work.

Competing interests

The authors declare no competing interests.

Additional information

Supplementary information is available for this paper at https://doi.org/10.1038/s41565-018-0297-6.

Reprints and permissions information is available at www.nature.com/reprints.

Correspondence and requests for materials should be addressed to N.M.L.

Publisher's note: Springer Nature remains neutral with regard to jurisdictional claims in published maps and institutional affiliations.

Methods

The topological photonic crystal slab was fabricated on a standard silicon-on-insulator wafer with a 270-nm-thick top silicon layer and a 3-μm-thick buried-oxide layer, using a standard fabrication technique[34]. The fabrication was done in two steps: (1) the top silicon layer of the silicon-on-insulator wafer was patterned using electron beam lithography with ZEP520A resist followed by reactive ion etching in CF_6 and C_4F_8 gases; and (2) photo-lithography with S1818 photo resist was used to define a window above the photonic crystal structure. Then, selective wet etching in buffered hydrofluoric acid was performed to remove the buried oxide under the photonic crystal (Supplementary Information, section D). Scanning electron microscopy images of the fabricated photonic crystal sample are shown in Supplementary Fig. 5f–h. The fabricated structure has a length of 82 unit cells and is 21 unit cells wide. The trapezoidally shaped defect has a height of 5 unit cells (in the y direction) and a top-side length of 10 unit cells (in the x direction), as illustrated in Fig. 3d–f.

To facilitate the comparison of propagation along trapezoidal and straight interfaces, the photonic crystal was designed in the following way. First, we compared two structures with the same dimensionality. Second, the left and right boundaries (along the y direction) of the photonic crystals were the same for both structures (see Fig. 3e and Supplementary Fig. 5g). Finally, the spacing in the y direction between the topological interface and the bulk silicon on the top and bottom was the same.

Our numerical simulations predict that the transverse profile of the edge state is antisymmetric with respect to the interface (as shown in Supplementary Fig. 4b). Therefore, the edge state is excited by the waveguide positioned slightly off-centre with respect to the interface between the two photonic crystals (see Fig. 3e), which allows for efficient excitation of this antisymmetric mode. An intermediate photonic crystal waveguide with a missing row of triangular air holes directly below the interface was used to further improve the light injection performance by reducing the mode-wave-vector mismatch and limiting scattering to the air. The overall achieved input-to-output coupling efficiency was estimated to be above 70% (Supplementary Information, section C).

The band structure of the photonic crystal slab (shown in Fig. 1b) and the dispersion relations for the edge states (shown in Fig. 2a) were calculated with full three-dimensional (3D) simulations using COMSOL Multiphysics software. The refractive index of silicon was taken as $n_{Si} = 3.48$. The remaining computations were performed in 2D configuration with the effective index of the silicon slab approximated as $n_{eff} = 2.965$ (Supplementary Information, section C). This assumption results in a small red-shift of the position of the Dirac cone and the band gap in the 2D photonic crystal compared with the original 3D structure (compare Fig. 2a and 2d). The plane wave expansion method, along with theoretical calculations using an effective Hamiltonian near the K/K' points, was used to compute the Berry curvature and Chern number shown in Fig. 1c (Supplementary Information, section B). The transmittance and normalized energy-density shown in Fig. 2c,d were simulated using COMSOL Multiphysics software. The finite-difference time-domain method (Lumerical) was used to calculate the transmittance spectra shown in Fig. 3b.

In the experiments, the input light from a 100 fs laser system with a repetition rate of 1 kHz (Coherent Libra) was coupled to an optical parametric amplifier (Light Conversion; TOPAS-C). The corresponding spectral full width at half maximum is approximately 40 nm at telecommunications wavelengths. The time interval between the generated pulses was 1 ms, ensuring that only one pulse at a time propagated through the sample, preventing interference effects resulting from an overlap between the two neighbouring pulses. Light was focused using an infinity corrected objective lens from free space onto the input grating followed by a taper to efficiently couple light into a single-mode silicon wire waveguide (see Fig. 3a and Supplementary Fig. 5f). Then, the energy was divided using a 50/50 Y-splitter, and half of the light was coupled to the photonic crystal, whereas the other half was transmitted through the silicon waveguide and used as a reference. The light transmitted through the photonic crystal and the reference light were out-coupled from the chip using diffraction gratings, and captured by the infrared camera. We designed the structure such that the input and output light had orthogonal polarizations, which enabled us to filter out all undesired input light reflected from the sample. A polarizer that transmitted only output-light polarization was used to eliminate unwanted orthogonally polarized light reflected from the sample. An InGaAs camera with an achromatic lens and objective lens, constituting a 4f system, was used for imaging. The use of an achromatic lens, microscope objective and pellicle beam splitter allowed for reliable measurements at a wide range of frequencies, reducing the chromatic aberrations.

Data availability

The data that support the plots within this paper and other findings of this study are available from the corresponding author upon reasonable request.

References

34. Reardon, C. P., Rey, I. H., Welna, K., O'Faolain, L. & Krauss, T. F. Fabrication and characterization of photonic crystal slow light waveguides and cavities. *J.Vis. Exp.* **69**, e50216 (2012).